PHILOSOPHICAL TRANSACTIONS A

rsta.royalsocietypublishing.org

Review

Article submitted to journal

Subject Areas:
Solar system, Fluid mechanics, Electromagnetism

Keywords:
Uranus, Neptune, ice giant planets, interiors, magnetic fields, dynamo

Author for correspondence:
Krista Soderlund
e-mail: krista@ig.utexas.edu

The Underexplored Frontier of Ice Giant Dynamos

K. M. Soderlund[1] and S. Stanley[2,3]

[1]Institute for Geophysics, John A. & Katherine G. Jackson School of Geosciences, The University of Texas at Austin, USA
[2]Department of Earth and Planetary Sciences, The Johns Hopkins University, Baltimore, MD, USA
[3]The Johns Hopkins University Applied Physics Laboratory, Laurel, MD, USA

The *Voyager 2* flybys of Uranus and Neptune revealed the first multipolar planetary magnetic fields and highlighted how much we have yet to learn about ice giant planets. In this review, we summarize observations of Uranus' and Neptune's magnetic fields and place them in context of other planetary dynamos. The ingredients for dynamo action in general and for the ice giants in particular are discussed, as are the factors thought to control magnetic field strength and morphology. These ideas are then applied to Uranus and Neptune, where we show that no models are yet able to fully explain their dynamos. We then propose future directions for missions, modeling, experiments, and theory necessary to answer outstanding questions about the dynamos of ice giant planets, both within our solar system and beyond.

THE ROYAL SOCIETY PUBLISHING

1. Introduction

As the solar system has been explored with spacecraft missions, our understanding of planetary magnetic fields has developed from the Earth as an archetypal example to learning about the large breadth of behaviors exhibited from Mercury to Neptune. Of the terrestrial planets, Mercury and Earth both have intrinsic magnetic fields at present as well as remnant crustal magnetization indicating long-lived magnetic activity (e.g., 1; 2; 3). Remnant fields on Mars and the Moon suggest they had intrinsic magnetic fields earlier in their histories, which have subsequently gone extinct (e.g., 4; 5). Meteorites suggest that active magnetic fields once existed on small bodies as well (e.g., 6). The magnetic history of Venus is not well constrained, but does not have an active field at present (e.g., 7; 8). Further out in the solar system, the giant planets as well as the Jovian satellite Ganymede all have intrinsic magnetic fields (e.g., 9; 10; 11; 12). Magnetic fields have been predicted theoretically for exoplanets (e.g., 13) and telescopic observations now enable their field strengths to be estimated (14; 15).

While our review is focused on the magnetic fields of Uranus and Neptune, it is important to put these in broader context, so we will first summarize the characteristics of planetary magnetic fields known at present. Figure 1 shows the surface radial magnetic fields of planets with intrinsic fields at present day. The Earth's magnetic field is dominated by the axial dipole component with a roughly 10 degree offset from the rotation axis. These large-scale field strengths reach about 100 μT. Mercury's magnetic field is similar in that the dominant field component is the axial dipole, but there are some clear differences. First, the dipole is offset northward so field in the northern hemisphere is stronger than that in the southern hemisphere. The magnetic and rotation axes are also aligned to within less than 1° of each other. And finally Mercury's field strength is almost two orders of magnitude weaker than Earth's field, with Mercury's field maximum of approximately 1 μT. The intrinsic magnetic field of Ganymede (not shown) also appears to be dipole-dominated with a small tilt of 4° and approximate field strength of 1 μT (12).

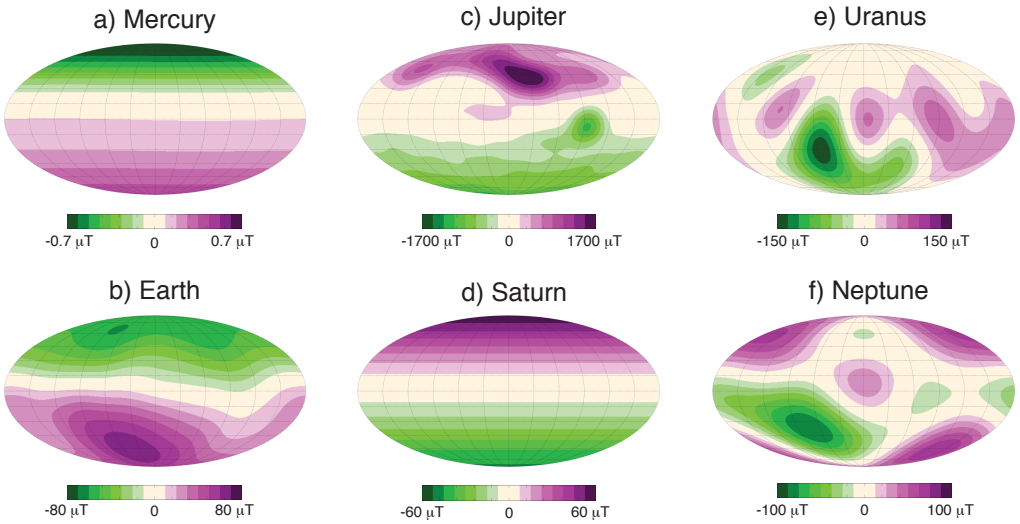

Figure 1. Radial magnetic field at the surfaces of a) Mercury, b) Earth, c) Jupiter, d) Saturn, e) Uranus, and f) Neptune. Data taken from (16) for Mercury (with spectral resolution of spherical harmonic degree $l \leq 5$), IGRF-13 coefficients are used for Earth and are available on the IAGA Division V-MOD Geomagnetic Field Modeling website ($l \leq 13$), (9) for Jupiter ($l \leq 10$), (17) for Saturn ($l \leq 11$), (18) for Uranus ($l \leq 4$), and (11) for Neptune ($l \leq 3$). The colors represent field intensity, where purple (green) indicates outward (inward) directed field. A mollweide projection is used in which the horizontal lines indicate constant latitude.

Considering the gas giants (Figure 1, panels c and d), Jupiter is dipole-dominated with a ~ 10 degree tilt between the magnetic and rotation axes. Field strengths are much larger, however, reaching more than 2000 μT at the 1 bar pressure level. The surface field is also more spatially complex than those of the terrestrial planets, with a high intensity band in the northern hemisphere, a strong flux patch near the equator, and fewer non-dipolar structures in the southern hemisphere. Downward continuation of the field shows these patterns remain generally intact to 0.85 Jovian radii (9; 19). Saturn is again dipole-dominated, with a nearly axisymmetric field like Mercury (tilt $< 0.007^\circ$) and surface field strengths similar to Earth's. Equatorial asymmetries do exist, however, with the magnetic equator located approximately 2800 km (~ 0.05 Saturnian radii) northward of the planetary equator. In addition, latitudinal banding is evident when downward continued to 0.75 Saturnian radii (17).

Finally, dramatically different magnetic fields are found at Uranus and Neptune (Figure 1, panels e and f). The fields are not dipole-dominated nor are they axially aligned. The dipole component is tilted by 59 degrees at Uranus and 47 degrees at Neptune. Since these magnetic fields have been measured only by single flybys of the *Voyager 2* spacecraft, only the largest scale components are well-resolved (e.g., dipole, quadrupole, and octupole), although smaller scale components can be constrained with special inversion techniques and assumptions of field complexity (11). Auroras at the magnetic field line footprints provide an additional constraint at Uranus, allowing the spherical harmonic degree $l = 4$ to also be estimated (18). It may, therefore, be expected that the planetary magnetic fields of Uranus and Neptune are likely to be considerably more detailed than existing observations reveal.

The maps in Figure 1 represent snapshots of the fields in time. However, magnetic fields evolve temporally, resulting in what is known as secular variation of the field. Evolution of the Earth's magnetic field has been tracked for more than 400 years, showing a slow westward drift of the field as well as changes in flux patches, where they wax and wane in field strength and shift locations (e.g., 20; 21). These variations can be used to estimate velocities of core flows (e.g., 22). Secular variation has also been measured at Jupiter by comparing magnetic field measurements taken by *Pioneer 10* and *11*, *Voyager 1*, *Ulysses*, and *Juno* missions between 1973 and 2018 (23); these changes are consistent with the advection of flux patches by zonal winds extending 5% down into the planet (23). At Mercury, no secular variation is evident between the *Mariner 10* mission in 1975 and the *MErcury Surface, Space ENvironment, GEochemistry, and Ranging (MESSENGER)* mission in 2014 (24); however, paleopole locations determined from crustal magnetic anomalies suggest that the dynamo has evolved with time (25). No detectable secular variation has been measured at Saturn over the thirty year period between the *Pioneer 11* and *Cassini* missions, with an upper bound of 2.8 nT/year (26). The single flybys of the *Voyager 2* spacecraft passed Uranus and Neptune prohibit any knowledge of their temporal variability.

These planetary magnetic fields fall into three broad categories, with important variations within each category. Mercury and Saturn have strikingly axisymmetric fields, with varying degrees of equatorial asymmetry between the northern and southern hemispheres that manifests as small to moderate offsets between the magnetic and planetary equators, and slow secular variation. Their field intensities, however, differ by nearly a factor of 100. Earth and Jupiter have dipole-dominated fields with $\sim 10^\circ$ tilts, prominent regions of enhanced intensities, and measured secular variation. Here, the field intensities vary by more than an order of magnitude. Ganymede's field is strongly dipolar with an intermediate dipole tilt and surface strength comparable to that of Mercury. Uranus and Neptune have multipolar fields with comparable intensities and have no clear symmetries along any axis. These observations lead to fundamental questions about planetary magnetic field generation: What processes control the magnetic field morphology, strength, and temporal evolution? What aspects of the planetary interiors are responsible for the variations we see across the terrestrial, gas giant, and ice giant planets as well as within each of these classes?

The paper is organized as follows: Section 2 reviews the fundamentals of planetary magnetic field generation, and Section 3 summarizes the factors controlling magnetic field strength and

morphology. Hypotheses to explain Uranus' and Neptune's unique magnetic fields are discussed in Section 4. Section 5 discusses future directions to advance our understanding of ice giant dynamos.

2. Magnetic Field Generation

Planetary magnetic fields are generated through self-sustained dynamo action, where motions in an electrically conducting fluid region of a planet act to maintain a magnetic field against decay from ohmic dissipation. This leads to several necessary conditions that must be met for a planet to sustain a dynamo. The most obvious is that the planet must have a fluid region that is both in motion and has an appreciable electrical conductivity.

Here we focus on some of the basics of planetary dynamo theory necessary for our discussion of ice giant dynamos. For a more complete overview of dynamo theory, see (27; 28). The fundamental equation for dynamo action is known as the Magnetic Induction Equation (MIE). It is derived by combining Maxwell's equations with Ohm's law in order to form a time evolution equation for magnetic field. For the special case of uniform electrical conductivity, the MIE becomes:

$$\frac{\partial \vec{B}}{\partial t} = \nabla \times \left(\vec{u} \times \vec{B} \right) + \eta \nabla^2 \vec{B} \tag{2.1}$$

where $\vec{B}$ is magnetic field, $\vec{u}$ is velocity, t is time, and $\eta = (\sigma \mu_0)^{-1}$ is magnetic diffusivity (which is inversely proportional to electrical conductivity σ and magnetic permeability μ_0).

Physical insight into dynamo action can be found by examining each term in the MIE. The left side of the equation represents how the magnetic field changes in time. The first term on the right side represents magnetic induction, i.e., how interactions between fluid motions and magnetic fields generate currents which can generate new magnetic field. This term can be seen as a source/sink term for the time evolution of the magnetic field. The second term on the right side represents ohmic diffusion. A dynamo is therefore a balance between induction and diffusion processes. In addition, note that the requirement that a dynamo needs fluid motions in an electrical conductor is a direct consequence of the MIE. If there are no fluid motions, then $\vec{u} = 0$ and we lose the only potential source term for generation of magnetic field. If the fluid is an electrical insulator, then $\sigma = 0$ and derivation of the MIE results in Laplace's equation $\nabla^2 \vec{B} = 0$.

A characteristic measure of dynamo action is given by comparing the magnitudes of the induction and diffusion terms on the right side of the MIE using representative estimates for the variables in these terms. Taking the ratio of the induction and diffusion terms gives a non-dimensional parameter known as the Magnetic Reynolds number: $Re_M = UL/\eta$, where U is a characteristic speed and L is a characteristic length-scale. A dynamo must maintain Re_M above a critical value in order for the dynamo to be sustained. Detailed mathematical treatments lead to lower bounds on $Re_{M,crit}$ of $\sim \pi$ or $\sim \pi^2$ depending on what choices are made for characteristic velocities. Numerical dynamo simulations typically find this value is $Re_{M,crit} \sim 20 - 40$.

Attaining a super-critical Re_M is necessary, but not sufficient, for maintaining a dynamo. Various anti-dynamo theorems (e.g., 29) demonstrate that fluid motions must maintain particular geometries. For example, the motions must be three-dimensional. This means that some of the fundamental fluid motions we expect in planets, such as solid body rotation and zonal flows cannot independently generate a dynamo because they do not possess a radial component. However, if a radial flow exists by other means, then differential rotation can contribute to dynamo generation. It can therefore be seen as a beneficial flow for magnetic field generation.

There are other fluid motions in planets that can produce the necessary radial motions for dynamo action. Most commonly appealed-to is convective motions due to buoyancy differences in the fluid. Convection may be thermal in origin if the temperature gradient in a region of the planetary interior is super-adiabatic, and/or it can be compositional in origin if a multi-component fluid is not miscible.

3. Magnetic Field Characteristics

A variety of tools are used to study the generation and characteristics of planetary magnetic fields and the fluid flows responsible for their generation, including theoretical arguments, numerical models, and laboratory experiments. These tools are often used together to develop scaling laws that allow a dynamo property, such as the strength and dipolarity of the magnetic field, to be estimated using fundamental properties of the planet (e.g., thickness of the dynamo region, rotation rate, fluid properties). Scaling laws also serve to relate numerical models and laboratory experiments to planetary interiors, whose extreme conditions cannot be replicated. Brief descriptions are given below and we refer the reader to other review papers for more details (e.g., 30; 31; 32; 33).

(a) Field Strength

Numerous scaling laws have been proposed to explain the characteristic magnetic field strength inside the dynamo region. Early studies suggested that the magnetic field strength would be set by the assumption of magnetostrophic balance between the Lorentz and Coriolis forces such that the dimensionless Elsasser number, $\Lambda = \sigma B^2/(\rho\Omega)$ where B is characteristic magnetic field strength, ρ is density, and Ω is rotation rate, is of order unity (e.g., 34). While this scaling is consistent with estimates for Earth and Jupiter (35), it does not work well in numerical dynamo models (e.g., 30; 36; 37) nor for Mercury or the ice giants.

Alternatively, scaling laws can be derived from the requirement that a dynamo must be thermodynamically consistent such that ohmic dissipation cannot exceed the energy available to drive the dynamo (38; 39). This approach with the assumption that the characteristic flow speed follows a mixing length scaling (obtained by balancing the nonlinear inertia and buoyancy forces) yields

$$\frac{B^2}{2\mu_0} = c f_{ohm} \rho^{1/3} \left(\frac{q_c R_c}{H_T}\right)^{2/3} \tag{3.1}$$

with constant prefactor c that has been shown empirically to be 0.63 (30), the fraction of ohmic to total dissipation f_{ohm} (typically ~ 0.5 in dynamo models, but ~ 1 may be more appropriate in planetary cores (31)), convective heat flux q_c, dynamo region radius R_c, temperature scale height $H_T = C_p/(\alpha g)$, specific heat capacity C_p, thermal expansion coefficient α, and gravitational acceleration g. This result, importantly, has no dependence on the rotation rate nor any diffusivity values. Assuming that magnetic energy depends only on convective power following turbulence theory, this expression can also be derived from first principles (i.e. no assumption for a velocity scaling) (33; 40).

Figure 2 shows how magnetic field strength scales with power for a collection of numerical dynamo models that span a wide range of parameter space (that do not overlap with planetary core estimates due to technological limitations (29)). With this power-based scaling law, the models roughly collapse onto a single power law and have a best fit exponent of 0.31, in reasonable agreement with the theoretical expectation of $1/3$ in equation 3.1. Moreover, $|B| \propto q_c^{1/3}$ holds approximately for both dipolar and multipolar dynamos (e.g., 42; 43), both stress-free and no-slip mechanical boundary conditions (e.g., 44), both fixed temperature and fixed flux thermal boundary conditions (e.g., 45), both Boussinesq and anelastic models (e.g., 43; 46), and different inner core sizes (e.g., 45). Thus, equation 3.1 appears to be a robust result that is supported by both theory and dynamo models.

In order to apply this scaling to planets, several additional steps are required. First, the depth to the top of the dynamo region must be assumed since the dipole field strength decreases with radius as r^3 and decreases even more rapidly for higher degree components. Second, the ratio of the mean field strength in the dynamo region to the field strength at the top of the dynamo region must be assumed since only the radial component is observable; dynamo models suggest the external field tends to be a factor of $3-4$ times smaller than the internal field (30). Third, the convective heat flux must be assumed, but is often poorly constrained. Figure 2b compares the

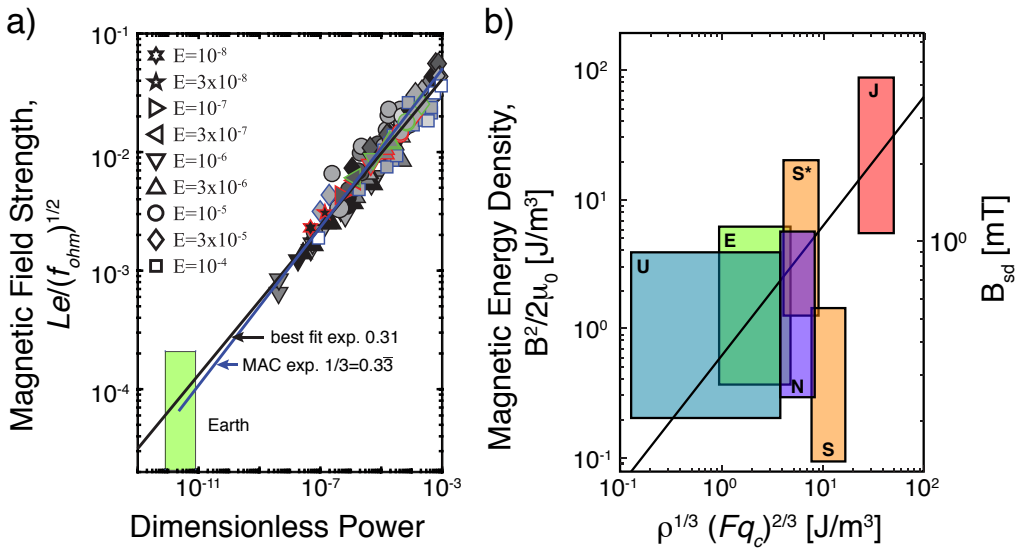

Figure 2. Magnetic field strengths for **a)** numerical dynamo models in dimensionless units and **b)** planetary interiors in dimensional units. In **a)**, black (blue) rimmed symbols denote thermal (compositional) convection cases from (30), red (green) rimmed symbols denote "coupled Earth" (standard) cases from (41). Symbol shape denotes the Ekman number, E (see legend). The gray scale denotes the magnetic Prandtl number, Pm, where white (black) indicates $Pm \geq 10$ ($Pm \leq 0.1$). Estimates for the geodynamo are in the green shaded box. $Le = B/((\rho\mu_0)^{1/2}\Omega L)$ is the Lehnert number, or the ratio of the periods of inertial and Alfvén waves. $E = \nu/(\Omega L^2)$ is the ratio of rotational to viscous timescales (ν is kinematic viscosity). $Pm = \nu/\eta$ is the ratio of magnetic to viscous diffusion timescales. In **b)**, field strength inside the dynamo region (at the planetary surface) is given on the left (right) y-axis. The x-axis includes an efficiency factor F that accounts for radial variations in fluid properties (39). The diagonal black line denotes the predicted behavior following equation 3.1. E denotes Earth, J denotes Jupiter, S denotes Saturn, S* denotes a deep-seated Saturnian dynamo, U denotes Uranus, and N denotes Neptune. Adapted from (32; 33).

magnetic field strength predictions of equation 3.1 against estimates for the geodynamo and giant planets. The predictions work well for the Earth and Jupiter, fall within the ranges of uncertainty for Uranus and Neptune, and do not match for Saturn unless a deep-seated dynamo is assumed. Thus, the scaling is also supported reasonably well by planetary estimates.

(b) Field Morphology

Numerical dynamo models are the primary tool for studying magnetic field morphology and have revealed numerous ways to generate multipolar magnetic fields. Magnetic field morphology is often characterized using dipolarity, f_{dip}, which measures the strength of the dipole component to the total field strength (e.g., 47) or to the combined field strength in spherical harmonic degrees 1 to 12 (e.g., 30; 48) on the outer boundary. For axial dipolarity, $f_{dip}^{m=0}$, the dipole component is limited to only the axisymmetric $m = 0$ contribution (e.g., 48). Early studies focused on the geodynamo typically assumed a Boussinesq fluid and considered a thick shell geometry, no-slip mechanical boundary conditions, and fixed temperature thermal boundary conditions such that buoyancy is concentrated along the inner boundary (termed "standard" models) (e.g., 36; 38; 49; 50). Near the onset of convection, stable dipole-dominated magnetic fields are obtained and the solutions transition to multipolar dynamos that evolve more rapidly in time as convective supercriticality is increased.

Non-linear inertia is found to play a ubiquitous role in the transition from dipole-dominated to multipolar magnetic fields (e.g., 36; 38; 42; 51; 52). Most frequently, inertia is compared against

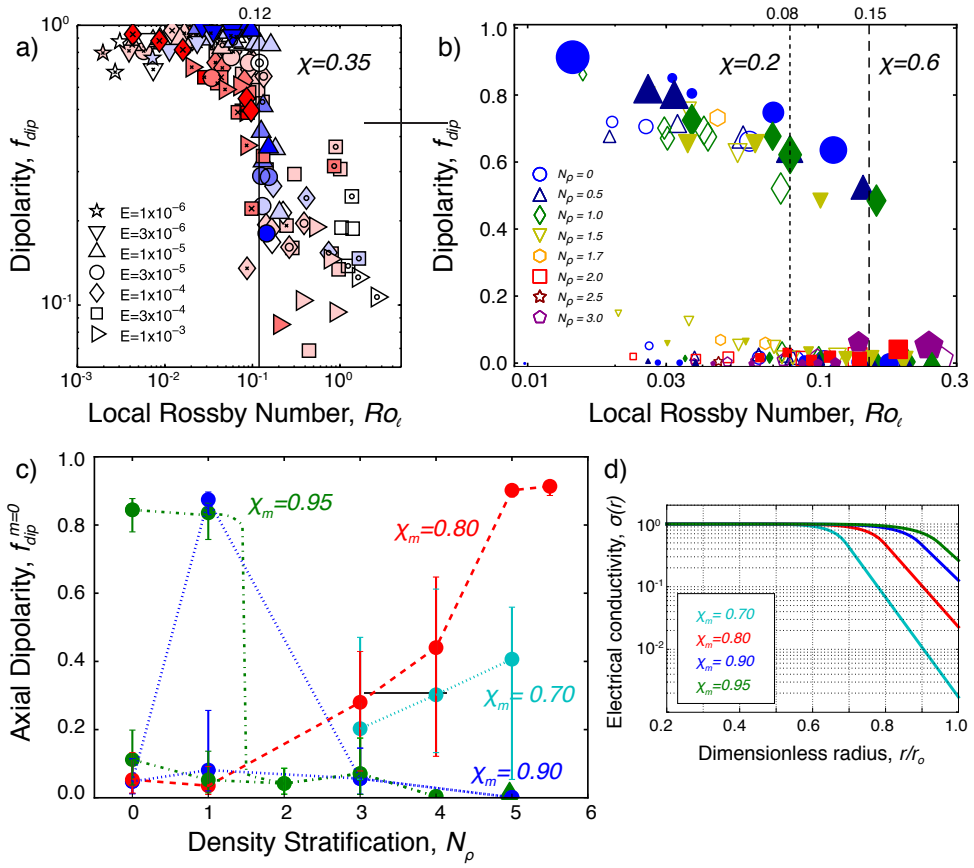

Figure 3. a) Dipolarity (based on magnetic field strength) versus the local Rossby number for standard dynamo models with a range of Ekman numbers (see legend). Interior color denotes Pm: blue $Pm < 1$, white $Pm = 1$, and red $Pm > 1$. Interior symbols denote the Prandtl number, $Pr = \nu/\kappa$ (ratio of thermal to viscous diffusion times, κ is thermal diffusivity): empty $Pr = 1$, cross $Pr > 1$, circle $Pr < 1$. Most cases have an electrically insulating inner core. Vertical line at $Ro_\ell = 0.12$ indicates the approximate transition between dipolar and multipolar dynamos. Adapted from (30). **b)** Dipolarity (based on magnetic energy) versus the local Rossby number for anelastic dynamo models with a range of density stratifications (see legend). Hollow (filled) symbols denote $\chi = 0.2$ ($\chi = 0.6$). Symbol size indicates magnetic field strength. Boundary conditions are fixed temperature and either no slip at the inner boundary and free slip at the outer boundary ("mixed") or stress-free at both boundaries. The inner core is electrically insulating. Vertical lines indicate the approximate transitions between dipolar and multipolar dynamos for $\chi = 0.2$ (short dash) and $\chi = 0.6$ (long dash). For panels b-c, $E = 10^{-4}$, $Pm = 2$, and $Pr = 1$. Adapted from (47). **c)** Axial dipolarity (based on magnetic energy) versus density stratification for anelastic dynamo models with $\chi = 0.2$ and the (dimensionless) radial electrical conductivity profiles shown in panel d. Boundary conditions are fixed temperature and mixed mechanical, and the inner core is electrically diffusive. Error bars correspond to standard deviations of the time series of each case. Adapted from (48).

the Coriolis force through a local Rossby number: $Ro_\ell = U/(\Omega\ell)$, where ℓ is the typical convective length scale. Figure 3a shows that dipole-dominated solutions are obtained when $Ro_\ell \lesssim 0.12$ in standard cases with $\chi = r_i/r_o = 0.35$ (ratio of inner to outer shell radii) for a wide range of input parameters, with multipolar dynamos occurring for larger Ro_ℓ values. The behavior becomes richer when stress-free boundary conditions and internal heating are considered. In particular, bistable solutions emerge where both dipolar and multipolar fields are obtained for the same input parameters and boundary conditions depending on the initial conditions (44; 53; 54; 55). This bistability is associated with the development of zonal winds, where dipolar solutions have

weak zonal winds and multipolar solutions are associated with strong winds. The range of magnetic field morphologies also becomes more exotic, including quadrupolar, oscillating, and hemispheric dynamos (53; 56; 57; 58). The dipolar-multipolar transition becomes less distinct when convection is driven by internal heating, but still roughly follows $Ro_\ell \sim 0.1$ (42; 45; 55).

Looking towards giant planets and stars, anelastic effects due to background density stratification as measured by the number of density scale heights, $N_\rho = \ln(\rho_i/\rho_o)$ where ρ_i and ρ_o are densities at the inner and outer boundaries respectively, are considered in Figure 3b. As for Boussinesq cases ($N_\rho = 0$), bistability is evident for stress-free boundary conditions (46; 47), which manifests as low dipolarity solutions within the low Ro_ℓ region. Excluding these bistable cases, the $Ro_\ell \sim 0.1$ transition criterion still appears to hold. Differences in shell thickness have a secondary influence, with the transition decreasing to $Ro_\ell \sim 0.08$ for thicker shells ($\chi = 0.2$) and increasing to $Ro_\ell \sim 0.15$ for thinner shells ($\chi = 0.6$). The addition of strong density stratification, however, can inhibit the generation of dipolar magnetic fields due to the concentration of convective features in the lower density region near the outer boundary (46; 47). No dipolar solutions are found for $N_\rho > 2$ by (47), although they can be recovered by increasing the magnetic Prandtl number (i.e. electrical conductivity) (46).

When electrical conductivity variations with radius are also incorporated, the behavior becomes even more complex and the $Ro_\ell \sim 0.1$ condition breaks down (48; 59; 60; 61; 62). Figure 3c shows how the electrical conductivity profile (Fig. 3d) modulates the magnetic field morphology as a function of density stratification. For small conductivity variations ($\chi_m > 0.9$), dipolar solutions are found only for small density stratifications ($N_\rho < 2$). For larger conductivity stratifications, the opposite behavior is found, where large density variations are required for dipolar solutions. This occurs because zonal winds become concentrated near the outer boundary, where interaction with the magnetic field is diminished.

Properties of the inner core, such as its electrical conductivity and relative size, may also influence the solutions (e.g., 63; 64)(cf. 65; 66). If electrically conducting and sufficiently large, the inner core can help maintain dipolar dynamos and decrease their reversal frequencies (e.g., 67; 68). Conversely, an insulating inner core or deep stably-stratified layer below the convecting fluid can prohibit anchoring of the dipole such that multipolar dynamos are preferred (67; 68; 69). A shallow stable layer above the convecting fluid tends to have the opposite effect and enhance the axisymmetry of the solutions (70; 71; 72; 73; 74), although a disruption of the dipole is also possible (75).

In summary, there are many paths to multipolar magnetic fields, such as strong inertial effects, bistability, strong density stratification, and deep stable layers. Application of these results to the ice giants is reviewed below.

4. Proposed Explanations for Ice Giant Dynamos

(a) Ice Giant Interiors

Uranus' and Neptune's magnetic fields tell us that there are regions inside the planets where electrically conductive fluids are undergoing dynamo-favorable motions. However, the lack of strong constraints on the ice giants' interior structure, composition, and thermal profiles limits our ability to determine exactly where inside Uranus and Neptune the dynamos are generated.

A recent review on the constraints and inferred interior structures of the ice giants can be found in (76). As a basic model, we can consider the ice giants as consisting of three layers: a relatively thin hydrogen-helium rich envelope, an ice-rich mantle, and a small rock-rich core, where the "-rich" intends to imply that small fractions of the other main components are likely present in each of the layers. However, high-pressure experiments and ab-initio simulations (e.g., 77; 78) demonstrate that the ice giant interiors are likely much more complicated than this simple three-layer structure. Icy materials such as water, ammonia, and methane (and their mixtures) have complex phase diagrams that we are only beginning to understand. Figure 4 demonstrates how complex the interiors may actually be.

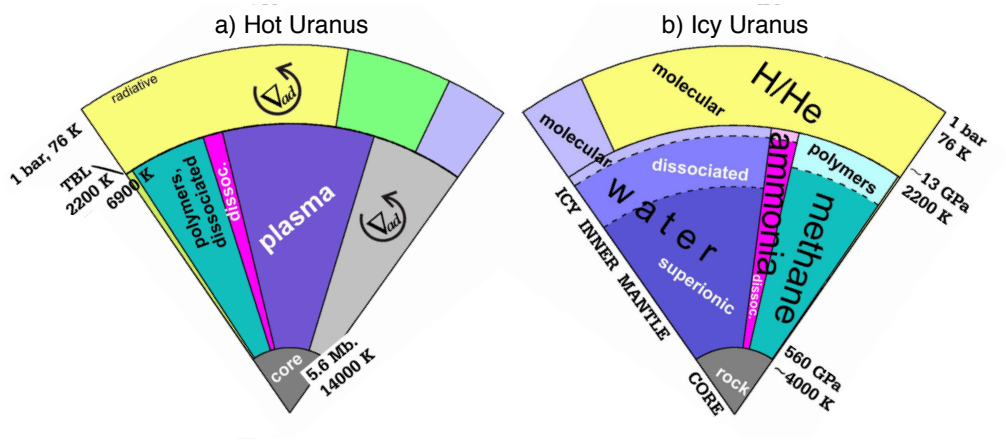

Figure 4. Three layer internal structure models for Uranus. **a)** 'Hot' Uranus model with an imposed thermal boundary layer (TBL) that fits gravity and luminosity data. **b)** 'Icy' Uranus model without a TBL using updated equations of state that fits gravity but not luminosity data. Adapted from (79; 80).

So how does one determine where the dynamo is generated in the ice giants? With present data and constraints, we are forced to use a combination of elimination and plausibility to answer this question. The hydrogen/helium envelope does not reach pressures high enough to attain strong electrical conductivity. The rocky core, although it may contain all the necessary ingredients for dynamo action, is likely too deep to explain the multipolar nature of Uranus' and Neptune's observed surface magnetic fields since the power in smaller-scale field components decays much more strongly with distance than the larger-scale (dipole) component. Eliminating those two layers leaves the ice-rich mantle layer. Considering water as an example of the ices making up the majority of Uranus and Neptune, the phase diagram suggests that appreciable conductivity can be reached at depths of $\sim 0.2 - 0.3$ planetary radii below the surface in Uranus and Neptune. At these depths, the conductivity is ionic in origin, and although ionic conductivity may be several orders of magnitude lower than the metallic conductivity of iron in the core, estimates of Re_M for the ice giants suggest that the conductivity is large enough for the ice-rich mantles to be super-critical to dynamo action.

(b) Multipolar field models

Several hypotheses were proposed to explain the unique magnetic field configurations of Uranus and Neptune revealed by the *Voyager 2* encounters. After the Uranus flyby, an ongoing reversal and the planet's large obliquity were hypothesized to be responsible (81; 82), but fell out of favor when the Neptune flyby also revealed a multipolar magnetic field. The large dipole tilts were additionally suggested to be related to a small number of large-scale convective cells in the interior (81; 83), and the lack of magnetostrophic balance between the Lorentz and Coriolis forces was suggested to explain why the weak ice giant fields differ from those of Earth and the gas giants (11). These arguments do not explain, however, why multipolar fields would be preferred. Deep, thin shell dynamos have also been proposed (potentially related to a metalized carbon layer below the ice layer) (84), but multipolar field morphologies at the surface are difficult to achieve due to the rapid attenuation of smaller-scale fields with radius. Thus, none of these early explanations are entirely satisfactory.

Shallow thin shell dynamos overlying a region of stable stratification were suggested by (85) to explain the low luminosities of Neptune and especially Uranus. Building upon this idea, Stanley and Bloxham (67; 69) carried out a suite of numerical dynamo simulations to test this hypothesis. Figure 5 compares dynamo simulations with solid inner cores of different sizes (indicated by χ)

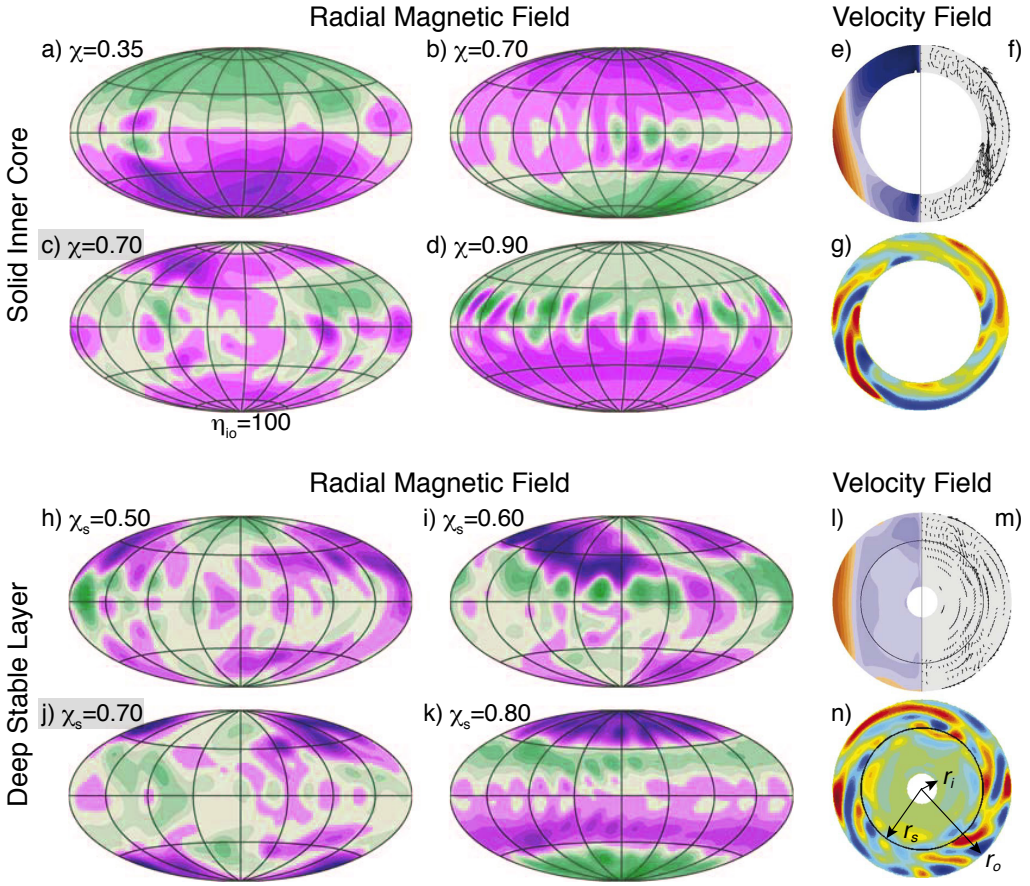

Figure 5. Magnetic and velocity fields in models with **a-g)** solid inner cores of different sizes given by $\chi = r_i/r_o$ and **h-n)** deep stable layers of different sizes given by $\chi_s = r_s/r_o$. **a-d, h-k)** Radial magnetic fields at the top of the dynamo region are instantaneous in time; colors denote field directions. **e, l)** Zonal flow snapshot averaged over all longitudes in the fluid layer corresponding to the models in panels c and j; orange (blue) denotes prograde (retrograde) flow. **f, m)** Meridional circulation flow vectors averaged over all longitudes. **g, n)** Axial vorticity, $\omega_z = \nabla \times \mathbf{u} \cdot \hat{\mathbf{z}}$, in the equatorial plane; red (blue) denotes cyclonic (anticyclonic) circulation. Input parameters are $E = 4 \times 10^{-5}(1-\chi)^{-2}$, $Pr = 1$, $Pm = 1$, and Ra varied such that all models produce similar magnetic field intensities of $\Lambda = \mathcal{O}(1)$. Boundary conditions are fixed flux and stress-free, the inner core/fluid has the same electrical conductivity as the outer fluid layer or is several orders of magnitude less. Adapted from (67).

and with deep stable layers of different thicknesses (indicated by $\chi_s = r_s/r_o$ where r_s is upper radius of the stable layer). Models with solid inner cores were only found to produce multipolar magnetic fields if the inner core is more magnetically diffusive (i.e. less electrically conducting) than the convecting fluid, as shown in panel c with $\eta_{io} = \eta_i/\eta_o = 100$ compared to panels a, b, and d with $\eta_{io} = 1$. In contrast, deep stable layers lead to ice giant-like magnetic fields in all models except for when the convecting layer is very thin (Fig. 5k). All models have field strengths of $\Lambda \sim 1$, which is much larger than the top of the dynamo region estimate of $\Lambda \sim 10^{-4}$ for the ice giants. The multipolar solutions are also found to evolve rapidly with time (advective time scales).

Considering the models with $\chi = 0.7$ (Fig. 5c) and $\chi_m = 0.7$ (Fig. 5j), convection is characterized by axial 'Taylor columns' that are aligned with the rotation axis (Fig. 5, panels g and n). The axisymmetric zonal (east-west) flows in both models are organized into a prograde (eastward) jet far from the rotation axis with retrograde (westward) flow at smaller cylindrical radii (Fig. 5, panels e and l). It should be noted that these models only simulated the dynamo

regions of the ice giants, i.e. they did not include the low-conductivity regions such as the molecular water region and gas-rich envelope. It is therefore not straightforward to compare the zonal winds in these models with those observed at the surfaces of Uranus and Neptune. It is nonetheless interesting to note that both the model and the planets' zonal winds are organized into a three jet structure, albeit with opposite directions (86). The axisymmetric meridional circulations have less defined structures (Fig. 5, panels f and m).

These models provide two possible mechanisms for generating ice giant-like magnetic fields: a solid inner core that is less electrically conductive than the overlying fluid shell or a deep stably-stratified layer beneath the convecting fluid shell. Although the properties of superionic ice are not well known (see Fig. 4), it is believed to behave as a solid (87) and to have an electrical conductivity exceeding that of ionic water (78), arguing against the first option. While the presence of a superionic ice layer would also argue against the second option, properties of the interior are sufficiently poorly constrained that stable stratification in the deep interior cannot be ruled out (76).

An alternative hypothesis is that the ice giants have multipolar dynamos because convective turbulence in their interiors is weakly constrained by rotation (i.e. inertial effects are strong), in contrast to rotationally constrained convection in the deep interiors of the gas giants that drives dipole-dominated dynamos (88; 89; 90). Figure 6 compares dynamo simulations with thick ($\chi = 0.35$) and thin ($\chi = 0.75$) shell geometries that are strongly driven to produce turbulent convection that is not organized into columnar structures (panels e and j). In both cases, the resulting magnetic fields are small scale and vary strongly with time. When limited to the largest spatial scales commensurate with observations ($l \leq 3$, panels b and g), multiple flux patches with different polarities are evident in both the northern and southern hemispheres with field strengths on the order of $\Lambda \sim 10^{-3}$, approaching agreement with the observations.

The models also produce retrograde equatorial jets that are accompanied by overturning circulations with upwelling at low latitudes and downwelling near the tangent cylinder (i.e. axial cylinder that intersects the inner boundary of the shell at the equator) (Fig. 6, panels c-d and h-i). Additional meridional circulations with polar upwellings develop if the spherical shell is thick. Strong prograde jets develop at smaller cylindrical radii in the thick shell, while the magnetic field decelerates the zonal flows in the thin shell dynamo case. These winds can, therefore, be similar qualitatively to those observed on Uranus and Neptune (86).

While this model seems promising, it is not yet clear if convection weakly constrained by rotation is likely in the ice giant interiors. This question is especially acute for Uranus, where the internal energy appears to be small (91).

Bistability has also been suggested as a possible explanation for why Uranus and Neptune have multipolar dynamos while Jupiter and Saturn have dipole-dominated magnetic fields (44; 47), which would require small local Rossby numbers for all four of the giant planets (42). The interplay between electrical conductivity and density stratification has not yet been investigated explicitly in the context of Uranus and Neptune (cf. **?**). Three-layer internal structure models suggest $N_\rho \sim 1.5$ for the water layer of Neptune ($0.30 - 0.85 R_N$) and $N_\rho \sim 1.3$ for Uranus ($0.18 - 0.78 R_U$) (92). Models with gradual compositional changes can have larger values of $N_\rho \sim 2.4$ for Uranus and $N_\rho \sim 1.9$ for Neptune considering the region extending from the center to 0.85 planetary radii (93). The electrical conductivity profile is not well constrained, but is expected to change by roughly an order of magnitude across the ionic water layer and more rapidly across the molecular envelope (94). Thus, both density and electrical conductivity stratifications appear to be moderate at depth, so this potential explanation requires further study.

In summary, numerous hypotheses have been proposed to explain the multipolar magnetic fields of Uranus and Neptune. However, in order to determine which - if any - of these explanations is correct, additional work is needed in regards to observational constraints as well as dynamo and rotating convection behavior as described in the next section.

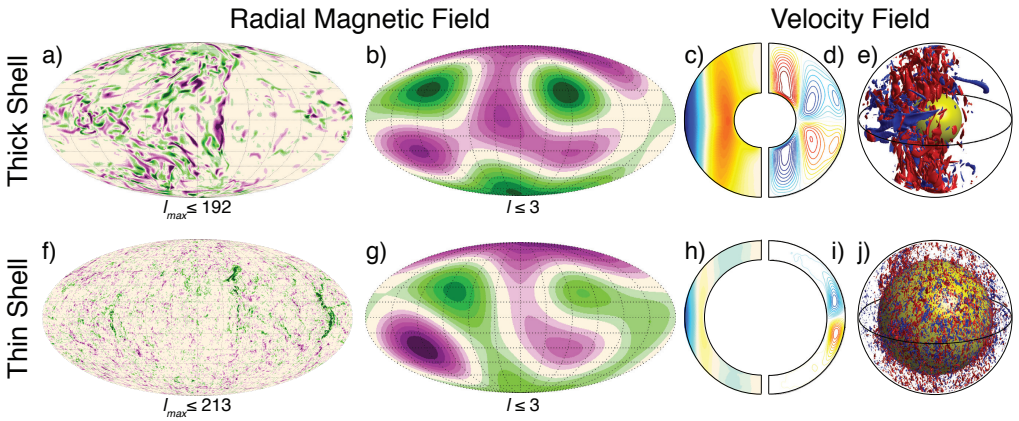

Figure 6. Magnetic and velocity fields in models with **a-e)** thick shells ($\chi = 0.35$) and **f-j)** thin shells ($\chi = 0.75$). **a-b, f-g)** Radial magnetic fields near the top of the dynamo region are instantaneous in time; colors denote field directions. Panels a and f are shown at full spatial resolutions; panels b and g are limited to spherical harmonic degrees $l \leq 3$. **c, h)** Zonal flow averaged over time and all longitudes in the fluid layer; red (blue) denotes prograde (retrograde) flow. **d, i)** Meridional circulations averaged over time and all longitudes; red (blue) denotes clockwise (counterclockwise) flows. **e, j)** Axial vorticity isosurfaces in the bulk fluid; the yellow sphere represents the solid inner core. Red (blue) denotes cyclonic (anticyclonic) ω_z values. Input parameters are $E = 3 \times 10^{-4}$, $Pr = 1$, $Pm = 1$, and $Ra = 2.22 \times 10^7$. Boundary conditions are isothermal and stress-free, and the outer fluid and solid inner core have the same electrical conductivity. Adapted from (89).

5. Future Directions

The planetary magnetic fields of our solar system show remarkable variations that reveal secrets about their deep interiors. The major revelations of the structure and dynamics of the interiors of Jupiter and Saturn from *Juno* and the *Cassini* Grand Finale, respectively, place our ignorance of ice giant interiors in stark contrast (e.g., 17; 95). Many questions remain about Uranus' and Neptune's interiors and magnetic fields, such as:

1. What are the detailed configurations of their magnetic fields? Has secular variation occurred since the *Voyager 2* flybys?
2. How deep do the atmospheric circulations observed on the surface extend into the interior and do they interact with the dynamo?
3. What is the internal density and compositional distribution? Do layers of stable stratification and/or double diffusion exist?
4. How do the thermodynamic and transport properties of the planets vary with radius?
5. What processes generate the dynamo? What are the characteristics of zonal winds, meridional circulations, and turbulent convective flows in the deep interior?
6. What are the dynamo characteristics of ice giant exoplanets? How do they compare to Uranus and Neptune, as well as to gas giant exoplanets and super-Earths?

The first three questions, in particular, illustrate the need for a new mission to Uranus and/or Neptune (e.g., 96). New magnetic field measurements close to the planet at a variety of latitudes and longitudes would allow characterization of the ice giants' higher degree magnetic field structure, ideally to better than spherical harmonic degree 10 for comparison with Earth, Jupiter, and Saturn and also to estimate the top of the dynamo region (e.g., 97). This field determination could be further improved through imaging of auroral and satellite footprints that provide additional high-latitude constraints (e.g., 18). The internal magnetic field may have undergone temporal change since the *Voyager 2* epoch so new observations, even from a flyby, would provide

constraints on secular variation and potentially identify changes in the locations of flux patches that are indicative of zonal and/or meridional winds in the deep interior (e.g., 23). The depth of zonal wind penetration into the planets as well as their radial density distributions may be established through measurements of the gravity field. Remote sensing would allow inference of deep meridional circulations, elemental abundances in the atmosphere, and internal heat flow. Observations of planetary oscillations might further constrain interior flows and identify layers of convection versus stable stratification (98). In situ measurements of winds, temperatures, and composition by a probe would ground truth for interpretations of the potential field and remote sensing observations.

The fourth question relies on advancements in planetary materials at high pressures and temperatures, coupled with interior structure models (e.g., 76). Equations of state are a necessary and critical ingredient of internal structure models that illustrate where the dynamo regions are likely located within the planets. The mode(s) and efficiency of heat transfer depend on thermodynamic properties, such as specific heat capacity, thermal conductivity, and thermal expansion coefficient, while the dynamics of convecting regions additionally depends on diffusivities (thermal, kinematic, and magnetic). Mean values of these properties are useful to estimate the dimensionless parameters that control convection and dynamo action (e.g., E, Pr, Pm, Re_M), and their variations with depth may also modulate magnetic field generation as described in Section 3.

Continued numerical modeling and laboratory experiments of convection and dynamo action are necessary for the fifth question, encompassing several directions. As new hypotheses for magnetic field generation progress with advancements in ice giant internal structures and physical properties, dynamo models provide a means to test these ideas. Dynamo model coupling with atmospheric dynamics and radiative transfer models would also be an interesting future direction. These models would make detailed predictions about magnetic fields, flow fields, and heat transfer that could serve to guide instrument and mission concept designs. Additionally, it is important to better understand and test convective regime transitions and their influence on magnetic field generation to answer questions like the feasibility of the ice giants being in the weakly rotating convective regime. As a last example, more realistic parameters (e.g., E, Pm) should be investigated as computing capabilities continue to improve with time since viscous effects may be (artificially) important in existing models (36) and novel behaviors are being found as new regions of parameter space are explored (e.g., 99).

Comparative planetology is another powerful tool to understand ice giant dynamos, per the sixth question. Exoplanets are routinely being discovered, with sub-Neptunes being among the most prominent (100). Recently, exoplanetary magnetic fields have been detected for the first time (15). Determining whether these planets have dipolar or multipolar dynamos and their zonal wind profiles would provide critical data points to assess dynamo generation hypotheses more broadly (e.g., 101). As we learn more about ice giant planets around other stars, we will also learn more about Uranus and Neptune closer to home.

Authors' Contributions. Both authors contributed to the writing of the manuscript.

Competing Interests. The authors declares that they have no competing interests.

Funding. This work was supported by the NASA Solar System Workings Program [grant numbers NNX15AL56G (KMS) and 80NSSC20K1046 (SS)].

Acknowledgements. We thank Mandy Bethkenhagen, Federica Coppari, Sebastien Hamel, Dustin Hill, Yong-Jae Kim, Marius Millot, Davina Spears, and Michael Wadas for stimulating discussions on ice giant interiors.

References

1 Panovska S, Constable CG, Korte M. 2018 Extending global continuous geomagnetic field reconstructions on timescales beyond human civilization. *Geochem. Geophys. Geosys.* **19**, 4757–4772.

2 Anderson BJ, Johnson CL, Korth H, Purucker ME, Winslow RM, Slavin JA, Solomon SC, McNutt RL Jr, Raines JM, Zurbuchen TH. 2011 The global magnetic field of mercury from messenger orbital observations. *Science* **30**, 1859–1862.

3 Johnson CL, Phillips RJ, Purucker ME, Anderson BJ, Byrne PK, Denevi BW, Feinberg JM, Hauck I S A, Head I J W, Korth H, James PB, Mazarico E, Neumann GA, Philpott LC, Siegler MA, Tsyganenko NA, Solomon SC. 2015 Low-altitude magnetic field measurements by MESSENGER reveal Mercury's ancient crustal field. *Science* **348**, 892–895.

4 Mittelholz A, Johnson CL, Feinberg JM, Langlais B, Phillips RJ. 2020 Timing of the martian dynamo: New constraints for a core field 4.5 and 3.7 Ga ago. *Science Advances* **6**, eaba0513.

5 Mighani S, Wang H, Shuster DL, Borlina CS, Nichols CIO, Weiss BP. 2020 The end of the lunar dynamo. *Science Advances* **6**, eaax0883.

6 Scheinberg A, Fu RR, Elkins-Tanton L, Weiss BP, Stanley S. 2017 Magnetic fields on asteroids and planetesimals. In *Planetesimals: Early Differentiation and Consequences for Planets*, pp. 180–203. Cambridge University Press.

7 Phillips JL, Russell CT. 1987 Upper limit on the intrinsic magnetic field of Venus. *J. Geophys. Res.* **92**, 2253–2263.

8 O'Rourke JG, Gillmann C, Tackley P. 2018 Prospects for an ancient dynamo and modern crustal remanent magnetism on Venus. *Earth Planet. Sci. Lett.* **502**, 46–56.

9 Connerney JEP, Kotsiaros S, Oliversen RJ, Espley JR, Jørgensen JL, Joergensen PS, Merayo JMG, Herceg M, Bloxham J, Moore KM, *et al.* 2018 A new model of Jupiter's magnetic field from Juno's first nine orbits. *Geophys. Res. Lett.* **45**, 2590–2596.

10 Dougherty MK, Cao H, Khurana KK, Hunt GJ, Provan G, Kellock S, Burton ME, Burk TA, Bunce EJ, Cowley SWH, *et al.* 2018 Saturn's magnetic field revealed by the Cassini Grand Finale. *Science* **362**, eaat5434.

11 Holme R, Bloxham J. 1996 The magnetic fields of Uranus and Neptune: Methods and models. *J. Geophys. Res.* **101**, 2177–2200.

12 Kivelson MG, Khurana KK, Volwerk M. 2002 The permanent and inductive magnetic moments of Ganymede. *Icarus* **157**, 507–522.

13 Driscoll PE, Olson PL. 2011 Optimal dynamos in the cores of terrestrial exoplanets: Magnetic field generation and detectability. *Icarus* **213**, 12–23.

14 Rogers TM. 2017 Constraints on the magnetic field strength of HAT-P-7 b and other hot giant exoplanets. *Nature Astron.* **1**, 1–4.

15 Cauley PW, Shkolnik EL, Llama J, Lanza AF. 2019 Magnetic field strengths of hot Jupiters from signals of star–planet interactions. *Nature Astron.* **3**, 1128–1134.

16 Thébault E, Langlais B, Oliveira JS, Amit H, Leclercq L. 2018 A time-averaged regional model of the Hermean magnetic field. *Phys. Earth Planet. Int.* **276**, 93–105.

17 Cao H, Dougherty MK, Hunt GJ, Provan G, Cowley SWH, Bunce EJ, Kellock S, Stevenson DJ. 2019 The landscape of Saturn's internal magnetic field from the Cassini Grand Finale. *Icarus* p. 113541.

18 Herbert F. 2009 Aurora and magnetic field of Uranus. *J. Geophys. Res. Space Physics* **114**.

19 Moore KM, Yadav RK, Kulowski L, Cao H, Bloxham J, Connerney JEP, Kotsiaros S, Jørgensen JL, Merayo JMG, Stevenson DJ, *et al.* 2018 A complex dynamo inferred from the hemispheric dichotomy of Jupiter's magnetic field. *Nature* **561**, 76–78.

20 Jackson A, Jonkers ART, Walker MR. 2000 Four centuries of geomagnetic secular variation from historical records. *Phil. Trans. R. Soc. A* **358**, 957–990.

21 Sabaka TJ, Olsen N, Purucker ME. 2004 Extending comprehensive models of the earth's magnetic field with ørsted and champ data. *Geophys. J. Int.* **159**, 521–547.

22 Livermore PW, Hollerbach R, Finlay CC. 2017 An accelerating high-latitude jet in Earth's core. *Nature Geosci.* **10**, 62–68.

23 Moore KM, Cao H, Bloxham J, Stevenson DJ, Connerney JEP, Bolton SJ. 2019 Time variation of Jupiter's internal magnetic field consistent with zonal wind advection. *Nature Astron.* **3**, 730–735.

24 Philpott LC, Johnson CL, Winslow RM, Anderson BJ, Korth H, Purucker ME, Solomon SC. 2014 Constraints on the secular variation of Mercury's magnetic field from the combined analysis of MESSENGER and Mariner 10 data. *Geoph* **41**, 6627–6634.

25 Oliveira JS, Hood LL, Langlais B. 2019 Constraining the early history of Mercury and its core dynamo by studying the crustal magnetic field. *J. Geophys. Res. Planets* **124**, 2382–2396.
26 Cao H, Russell CT, Christensen UR, Dougherty MK, Burton ME. 2011 Saturn's very axisymmetric magnetic field: No detectable secular variation or tilt. *Earth Planet. Sci. Lett.* **304**, 22–28.
27 Roberts P. 2007 Theory of the Geodynamo. In *Treatise on Geophysics* (ed. G Schubert), chapter 8.03. Elsevier.
28 Desjardins B, Dormy E, Gilbert A, Proctor M. 2007 Introduction to self-excited dynamo action. In *Mathematical Aspects of Natural Dynamos* (ed. E Dormy, A Soward), chapter 1. Chapman and Hall/CRC.
29 Roberts PH, King EM. 2013 On the genesis of the Earth's magnetism. *Rep. Prog. Phys.* **76**, 096801.
30 Christensen UR. 2010 Dynamo scaling laws and applications to the planets. *Space Sci. Rev.* **152**, 565–590.
31 Jones CA. 2011 Planetary magnetic fields and fluid dynamos. *Annu. Rev. Fluid Mech.* **43**, 583–614.
32 Christensen UR. 2019 Planetary Magnetic Fields and Dynamos. In *Oxford Research Encyclopedia of Planetary Science*.
33 Wicht J, Sanchez S. 2019 Advances in geodynamo modelling. *Geophys. Astrophys. Fluid Dyn.* **113**, 2–50.
34 Stevenson DJ. 1979 Turbulent thermal convection in the presence of rotation and a magnetic field: A heuristic theory. *Geophys. Astrophys. Fluid Dyn.* **12**, 139–169.
35 Stevenson DJ. 2003 Planetary magnetic fields. *Earth Planet. Sci. Lett.* **208**, 1–11.
36 Soderlund KM, King EM, Aurnou JM. 2012 The influence of magnetic fields in planetary dynamo models. *Earth Planet. Sci. Lett.* **333-334**, 9–20.
37 Soderlund KM, Sheyko A, King EM, Aurnou JM. 2015 The competition between Lorentz and Coriolis forces in planetary dynamos. *Prog. Earth Planet. Sci.* **2**, 24.
38 Christensen UR, Aubert J. 2006 Scaling properties of convection driven dynamos in rotating spherical shells and application to planetary magnetic fields. *Geophys. J. Int.* **166**, 97–114.
39 Christensen UR, Holzwarth V, Reiners A. 2009 Energy flux determines magnetic field strength of planets and stars. *Nature* **457**, 167–169.
40 Davidson PA. 2013 Scaling laws for planetary dynamos. *Geophys. J. Int.* **195**, 67–74.
41 Aubert J, Gastine T, Fournier A. 2017 Spherical convective dynamos in the rapidly rotating asymptotic regime. *J. Fluid Mech.* **813**, 558–593.
42 Olson PL, Christensen UR. 2006 Dipole moment scaling for convection-driven planetary dynamos. *Earth Planet. Sci. Lett.* **250**, 561–571.
43 Yadav RK, Gastine T, Christensen UR, Duarte L. 2013 Consistent scaling laws in anelastic spherical shell dynamos. *ArXiv e-prints* .
44 Yadav RK, Gastine T, Christensen UR. 2013 Scaling laws in spherical shell dynamos with free-slip boundaries. *Icarus* **225**, 185–193.
45 Aubert J, Labrosse S, Poitou C. 2009 Modelling the palaeo-evolution of the geodynamo. *Geophys. J. Int.* **179**, 1414–1428.
46 Schrinner M, Petitdemange L, Raynaud R, Dormy E. 2014 Topology and field strength in spherical, anelastic dynamo simulations. *Astron. Astrophys.* **564**, A78.
47 Gastine T, Duarte L, Wicht J. 2012 Dipolar versus multipolar dynamos: the influence of the background density stratification. *Astron. Astrophys.* **546**, A19.
48 Duarte L, Gastine T, Wicht J. 2013 Anelastic dynamo models with variable electrical conductivity: an application to gas giants. *Phys. Earth Planet. Int.* **222**, 22–34.
49 Olson PL, Christensen UR, Glatzmaier GA. 1999 Numerical modeling of the geodynamo: Mechanisms of field generation and equilibration. *J. Geophys. Res.* **104**, 10383–10404.
50 Christensen UR, Olson PL, Glatzmaier GA. 1999 Numerical modeling of the geodynamo: A systematic parameter study. *Geophys. J. Int.* **138**, 393–409.
51 Sreenivasan B, Jones CA. 2006 The role of inertia in the evolution of spherical dynamos. *Geophys. J. Int.* **164**, 467–476.

52 Oruba L, Dormy E. 2014 Transition between viscous dipolar and inertial multipolar dynamos. *Geophys. Res. Lett.* **41**, 7115–7120.
53 Simitev RD, Busse FH. 2009 Bistability and hysteresis of dipolar dynamos generated by turbulent convection in rotating spherical shells. *Europhys. Lett.* **85**, 19001.
54 Schrinner M, Petitdemange L, Dormy E. 2012 Dipole collapse and dynamo waves in global direct numerical simulations. *Astrophys. J.* **752**, 121.
55 Dharmaraj G, Stanley S, Qu AC. 2014 Scaling laws, force balances and dynamo generation mechanisms in numerical dynamo models: influence of boundary conditions. *Geophys. J. Int.* **199**, 514–532.
56 Grote E, Busse FH, Tilgner A. 2000 Regular and chaotic spherical shell dynamos. *Phys. Earth Planet. Int.* **117**, 259–272.
57 Kutzner C, Christensen UR. 2000 Effects of driving mechanisms in geodynamo models. *Geophys. Res. Lett.* **27**, 29–32.
58 Kutzner C, Christensen UR. 2002 From stable dipolar towards reversing numerical dynamos. *Phys. Earth Planet. Int.* **131**, 29–45.
59 Jones CA. 2014 A dynamo model of Jupiter's magnetic field. *Icarus* **241**, 148–159.
60 Duarte LD, Wicht J, Gastine T. 2018 Physical conditions for Jupiter-like dynamo models. *Icarus* **299**, 206–221.
61 Dietrich W, Jones CA. 2018 Anelastic spherical dynamos with radially variable electrical conductivity. *Icarus* **305**, 15–32.
62 Wicht J, Gastine T, Duarte LDV. 2019 Dynamo Action in the Steeply Decaying Conductivity Region of Jupiter-Like Dynamo Models. *J. Geophys. Res. Planets* **124**, 837–863.
63 Hollerbach R, Jones CA. 1993 Influence of the Earth's inner core on geomagnetic fluctuations and reversals. *Nature* **365**, 541–543.
64 Heimpel MH, Aurnou JM, Al-Shamali F, Gomez Perez N. 2005 A numerical study of dynamo action as a function of spherical shell geometry. *Earth Planet. Sci. Lett.* **236**, 542–557.
65 Wicht J. 2002 Inner-core conductivity in numerical dynamo simulations. *Phys. Earth Planet. Int.* **132**, 281–302.
66 Busse FH, Simitev RD. 2008 Toroidal flux oscillation as possible cause of geomagnetic excursions and reversals. *Phys. Earth Planet. Int.* **168**, 237–243.
67 Stanley S, Bloxham J. 2006 Numerical dynamo models of Uranus' and Neptune's unusual magnetic fields. *Icarus* **184**, 556–572.
68 Dharmaraj G, Stanley S. 2012 Effect of inner core conductivity on planetary dynamo models. *Phys. Earth Planet. Int.* **212–213**, 1–9.
69 Stanley S, Bloxham J. 2004 Convective-region geometry as the cause of Uranus' and Neptune's magnetic fields. *Nature* **428**, 151–153.
70 Christensen UR. 2006 A deep dynamo generating Mercury's magnetic field. *Nature* **444**, 1056–1058.
71 Christensen UR, Wicht J. 2008 Models of magnetic field generation in partly stable planetary cores: Applications to Mercury and Saturn. *Icarus* **196**, 16–34.
72 Stanley S. 2010 A dynamo model for axisymmetrizing Saturn's magnetic field. *Geophys. Res. Lett.* **37**, L05201.
73 Nakagawa T. 2011 Effect of a stably stratified layer near the outer boundary in numerical simulations of a magnetohydrodynamic dynamo in a rotating spherical shell and its implications for Earth's core. *Phys. Earth Planet. Int.* **187**, 342–352.
74 Christensen UR. 2015 Iron snow dynamo models for Ganymede. *Icarus* **247**, 248–259.
75 Stanley S, Mohammadi A. 2008 Effects of an outer thin stably stratified layer on planetary dynamos. *Phys. Earth Planet. Int.* **168**, 179–190.
76 Helled R, Nettelmann N, Guillot T. 2020 Uranus and Neptune: Origin, Evolution and Internal Structure. *Space Sci. Rev.* **216**, 1–26.
77 French M, Becker A, Lorenzen W, Nettelmann N, Bethkenhagen M, Wicht J, Redmer R. 2012 Ab initio simulations for material properties along the Jupiter adiabat. *Astrophys. J. Supp.* **202**, 5.
78 Millot M, Hamel S, Rygg JR, Celliers PM, Collins GW, Coppari F, Fratanduono DE, Jeanloz R, Swift DC, Eggert JH. 2018 Experimental evidence for superionic water ice using shock compression. *Nature Physics* **14**, 297–302.

79 Nettelmann N, Wang K, Fortney JJ, Hamel S, Yellamilli S, Bethkenhagen M, Redmer R. 2016 Uranus evolution models with simple thermal boundary layers. *Icarus* **275**, 107–116.

80 Bethkenhagen M, Meyer ER, Hamel S, Nettelmann N, French M, Scheibe L, Ticknor C, Collins LA, Kress JD, Fortney JJ, *et al.* 2017 Planetary ices and the linear mixing approximation. *Astrophys. J.* **848**, 67.

81 Connerney JEP, Acuna M, Ness NF. 1987 The magnetic field of Uranus. *J. Geophys. Res.* **92**, 15329–15336.

82 Schulz M, Paulikas GA. 1990 Planetary magnetic fields: A comparative view. *Adv. Space Res.* **10**, 55–64.

83 Connerney JEP, Acuna MH, Ness NF. 1991 The magnetic field of neptune. *J. Geophys. Res. Space Physics* **96**, 19023–19042.

84 Ruzmaikin AA, Starchenko SV. 1991 On the origin of Urains and Neptune magnetic fields. *Icarus* **93**, 82–87.

85 Hubbard WB, Podolak M, Stevenson DJ. 1995 Interior of Neptune. In *Neptune and Triton* (ed. Cruickshank, D). Tucson: University of Arizona Press.

86 Fletcher LN, de Pater I, Orton GS, Hofstadter MD, Irwin PGJ, Roman MT, Toledo D. 2020 Ice giant circulation patterns: Implications for atmospheric probes. *Space Sci. Rev.* **216**, 1–38.

87 Millot M, Coppari F, Rygg JR, Barrios AC, Hamel S, Swift DC, Eggert JH. 2019 Nanosecond X-ray diffraction of shock-compressed superionic water ice. *Nature* **569**, 251–255.

88 Aurnou JM. 2007 Planetary core dynamics and convective heat transfer scaling. *Geophys. Astrophys. Fluid Dyn.* **101**, 327–345.

89 Soderlund KM, Heimpel MH, King EM, Aurnou JM. 2013 Turbulent models of ice giant internal dynamics: Dynamos, heat transfer, and zonal flows. *Icarus* **224**, 97–113.

90 King EM, Aurnou JM. 2013 Turbulent convection in liquid metal with and without rotation. *Proc. Natl. Acad. Sci.* **110**, 6688–6693.

91 Ingersoll AP. 1999 *Atmospheres of the giant planets*. Cambridge University Press.

92 Nettelmann N, Helled R, Fortney JJ, Redmer R. 2013 New indication for a dichotomy in the interior structure of Uranus and Neptune from the application of modified shape and rotation data. *Planet. Space Sci.* **77**, 143–151.

93 Helled R, Anderson JD, Podolak M, Schubert G. 2011 Interior models of uranus and neptune. *Astrophys. J.* **726**, 15–22.

94 Redmer R, Mattsson TR, Nettelmann N, French M. 2011 The phase diagram of water and the magnetic fields of Uranus and Neptune. *Icarus* **211**, 798–803.

95 Stevenson DJ. 2020 Jupiter's Interior as Revealed by Juno. *Annu. Rev. Earth Planet. Sci.* **48**.

96 Hofstadter MD, Simon A, Reh K, Elliot J. 2017 Ice giants pre-decadal study final report. *Rept. D-100520, Jet Propulsion Lab., Pasadena, CA* .

97 Tsang YK, Jones CA. 2020 Characterising Jupiter's dynamo radius using its magnetic energy spectrum. *Earth Planet. Sci. Lett.* **530**, 115879.

98 Friedson AJ. 2020 Ice giant seismology: Prospecting for nonradial oscillations. *Phil. Trans. R. Soc. A* **this volume**.

99 Aurnou JM, Calkins MA, Cheng JS, Julien K, King EM, Nieves D, Soderlund KM, Stellmach S. 2015 Rotating convective turbulence in earth and planetary cores. *Phys. Earth Planet. Int.* **246**, 52–71.

100 Borucki WJ. 2017 Kepler: A brief discussion of the mission and exoplanet results. *Proc. Am. Phil. Soc.* **161**, 38.

101 Tian B, Stanley S. 2012 Interior Structure of Water Planets: Implications for their dynamo source regions. *Astrophys. J.* **768**, 156.